



The behaviour of aluminium, manganese, iron, cobalt, and lead in the subarctic Pacific Ocean: boundary scavenging and temporal changes

Cheuk-Yin Chan¹ · Linjie Zheng¹ · Yoshiki Sohrin¹

Received: 2 June 2023 / Revised: 4 December 2023 / Accepted: 9 December 2023 / Published online: 13 January 2024
© The Author(s) 2024

Abstract

Aluminium (Al), manganese (Mn), iron (Fe), cobalt (Co), and lead (Pb) are trace metals that exhibit significant scavenging tendencies in the oceans. This study presents the full-depth distributions of the dissolved (d) and labile particulate (lp) fractions of these five elements in the subarctic Pacific Ocean, obtained during the GEOTRACES Japan KH-17-3 cruise. Along the 145° W meridional transect, the d and lp species of Al, Mn, Fe, and Co reflected fluvial supply from Alaska and benthic input from the continental shelf. We estimated that the boundary-scavenging zone has a width of approximately 250 km off Alaska. Along the 47° N zonal transect (GEOTRACES GP02 Line), we found input of trace metals from the Okhotsk and Bering Seas in the west, contrasting to the limited input of trace metals due to boundary scavenging in the east. The hydrothermal activity of the Juan de Fuca Ridge influenced the distribution of deep-water trace metals at the easternmost station, CL-21. Temporal change in the vertical profiles of dPb in the middle of the subarctic gyre highlighted a decline in anthropogenic Pb emissions from 2005 to 2017. Temporal change of the vertical profiles of Al, Mn, and Fe at 47° N, 160° E from 2011 to 2017 indicates the influence of the Great East Japan Earthquake. In particular, lp trace metals were brought by tsunami and ocean circulation in 2011, and decreased over time through scavenging.

Keywords GEOTRACES · Trace metals · Labile particulate species · Boundary scavenging · Anthropogenic pollution · Temporal change

1 Introduction

Aluminium (Al), manganese (Mn), iron (Fe), cobalt (Co), and lead (Pb) are trace metals that exhibit significant scavenging tendencies in the oceans. Al, Mn, Co, and Pb are classified as scavenged-type elements (Bruland and Lohan 2003; Chester 2009), and their dissolved concentration generally decreases with increasing depth. These scavenged-type elements have a relatively short residence time because they are adsorbed by particles, and their concentration increases near

the sources. Fe is classified as a hybrid of scavenged-type and nutrient-type element, as Fe is depleted in surface water by phytoplankton uptake and is influenced by remineralisation and scavenging in intermediate and deep waters (Zheng and Sohrin 2019). Classical studies on these five trace metals have been summarised in our previous papers (Zheng et al. 2019, 2022; Zheng and Sohrin 2019). Here, we describe recent studies in the subarctic Pacific that is an area of high-nutrient low-chlorophyll (HNLC) and an end point of global thermohaline circulation.

Nishioka et al. (2020) reported the distribution of dissolved (d) Fe along the 47° N GEOTRACES GP02 section during the GEOTRACES Japan KH-17-3 cruise. Combined with previous results, they emphasised the importance of dFe supply from marginal seas, such as the western Bering Sea and Okhotsk Sea. They also suggested that the North Pacific Intermediate Water (NPIW) links deep and surface waters, supplying nutrients and dFe to surface water and contributing to biological production. Wong et al. (2022) also analysed samples collected from the KH-17-3 cruise

✉ Cheuk-Yin Chan
chan.cheukyin.78s@st.kyoto-u.ac.jp

Linjie Zheng
zheng.linjie.7w@kyoto-u.ac.jp

Yoshiki Sohrin
sohrin@scl.kyoto-u.ac.jp

¹ Institute for Chemical Research, Kyoto University, Uji, Kyoto 611-0011, Japan

to determine the concentrations of dMn and dFe. They suggested that dMn and dFe are transported eastward in intermediate waters and that dMn transport distance is the longest in the Pacific. Sim and Orians (2019) reported the annual variability of dMn along Line-P in the Northeast Pacific, and the remobilization of dMn from the continental slope was found to be a significant source. Chmiel et al. (2022) reported the distribution of dCo along the 150° W GEOTRACES GP15 section. Michael et al. (2023) analysed unfiltered samples for total dissolvable (td) fraction, and reported that glacial meltwater and sediment resuspension are important sources of dissolved and total dissolvable Al and Mn in coastal surface waters of the Gulf of Alaska.

Compared with dissolved species, there are few studies on particulate species. Particles which control the distribution of trace metals in the water column have been transported externally or produced internally (Lam et al. 2015b). External sources such as atmospheric dust deposition, fluvial inputs, and sediment resuspension release lithogenic particles into seawater. Aerosols bring anthropogenic inputs to the ocean, such as Pb. However, internal processes such as biological production and authigenic mineral precipitation produce different types of particles. As a result, ocean particles are composed of organic matter, biogenic calcium carbonate and opal, Fe–Mn oxyhydroxides, and lithogenic materials (Lam et al. 2015a). In hydrothermal plumes, Fe–Mn oxyhydroxides are important scavenging particulates (German and Von Damm 2003). Dissolved trace metals such as Al, Mn, Fe, and Co are adsorbed onto the particle surface, then removed when the particles aggregate and sink (Lamborg et al. 2008). The adsorption of trace metals onto the particle surface is controlled by surface complexation, resulting in various scavenging residence times for trace metals (Balistrieri et al. 1981; Li 1981). At ocean margins, some scavenged-type trace elements are removed from seawater at a faster rate than in the open ocean. This phenomenon has been termed “boundary scavenging” (Spencer et al. 1981) and has been studied predominantly by using

radionuclides, such as lead-210 and protactinium-231 (Anderson et al. 1990; Bacon et al. 1976).

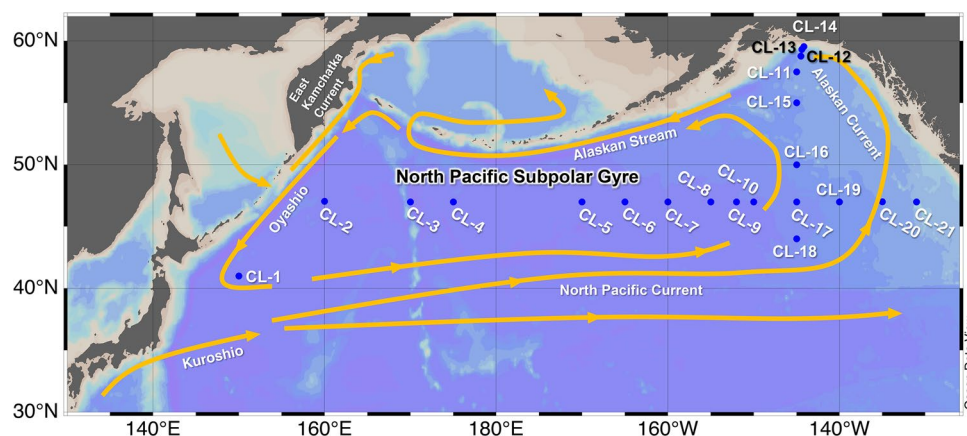
The specific goals of this study are to identify major processes that control the distribution of trace metals in the subarctic Pacific based on multielemental analysis. We investigated the distribution of Al, Mn, Fe, Co, and Pb in the North Pacific Ocean, mainly along the 160° W meridional section (GEOTRACES GPc06) (Zheng et al. 2019) (Zheng and Sohrin 2019). We determined d and td concentrations of these five elements by analysing filtered and unfiltered seawater samples, respectively. Labile particulate (lp) concentration was calculated as the difference between td and d concentrations. We evaluated the boundary scavenging off the Aleutian Islands using the integral concentrations of Al, Mn, and Fe. Due to poor weather conditions, we did not complete the GEOTRACES GP02 zonal section along 47°N during the GEOTRACES Japan KH-12-4 cruise in 2012. In this study, we report the distribution of five trace metals during the GEOTRACES Japan KH-17-3 cruise. We analyse the full-depth distribution along the GP02 section and discuss the east–west gradients of trace metals on an isopycnal surface. We evaluate boundary scavenging along 145°W in the Gulf of Alaska. In addition, we investigate temporal changes in dPb concentration in the middle of the subarctic gyre. We also study temporal changes in d and lp concentrations at 47°N, 160°E after the Great East Japan Earthquake.

2 Methods

2.1 Study area

Seawater samples were collected during the GEOTRACES Japan KH-17-3 cruise of the R/V *Hakuho Maru* from 23 June to 9 August 2017. Figure 1 shows the locations of the sampling stations and surface currents in the subarctic Pacific Ocean. The stations are located along an east–west transect along 47°N (GEOTRACES GP02 section) and a

Fig. 1 Map of sampling stations during the R/V *Hakuho Maru* KH-17-3 cruise. Major ocean currents are indicated by orange arrows (color figure online)



north–south transect along 145°W in the Gulf of Alaska. Along the GP02 section, three stations were revisited: stations CL-2, CL-3, and CL-5 of the KH-17-3 cruise, correspond to BD-7, BD-9, and BD-14 of the KH-12-4 cruise, respectively (Zheng et al. 2019). Station CL-14 (59.55° N, 144.16° W; 695 m) was closest to the continent (approximately 50 km off the coast).

2.2 Sampling

Seawater samples were collected using a clean sampling system (Sohrin and Bruland 2011) during the KH-17-3 cruise. The carousel sampling system (SBE-32, Sea-Bird Scientific, USA) was equipped with conductivity, temperature, and depth (CTD) sensors (SEB-9-Plus, Sea-Bird Scientific) and 24 Niskin-X bottles (12 L, General Oceanics, USA). The Niskin-X bottles were pre-cleaned internally with 1% Extran MA01 detergent (Merck Millipore, USA), 0.1 mol/kg HCl, and ultrapure Milli-Q water (MQW) successively at the beginning of the cruise, according to the Sampling and Sample-handling Protocols for GEOTRACES Cruises (Cutter et al. 2017). After sampling, the Niskin-X bottles were immediately placed in a clean bubble with two high-efficiency particulate air (HEPA) filter units in an onboard laboratory. Inside the clean bubble, seawater samples for dissolved metal (dM) analysis were filtered through a 0.2/0.8 µm pore size AcroPak 200 filter (Pall Industries, USA), and collected in acid-cleaned 250 mL Nalgene low density polyethylene (LDPE) bottles (Thermo Fisher Scientific, USA). Seawater samples for total dissolvable metal (tdM) analysis were collected directly in LDPE bottles without filtration. All samples were acidified onboard with Optima HCl (Thermo Fisher Scientific, USA) to a pH of ~1.9, and stored at ambient temperature for at least two years until analysis.

2.3 Analysis

To pre-concentrate Al, Mn, Fe, Co, Ni, Cu, Zn, Cd, and Pb in the seawater samples, an automated solid-phase extraction system SPE-100 (Hiranuma Sangyo, Japan) equipped with a Nobias Chelate-PA1 resin column (Hitachi High Technologies, Japan) was used (Minami et al. 2015). Just before preconcentration, the pH of seawater samples was adjusted to 6.00 ± 0.05 by adding 3.6 mol/kg HAcO-NH₄AcO (acetic acid-ammonium acetate) buffer solution, which was prepared from Optima glacial HAcO and TAMAPURE AA-10 NH₃ (Tama Chemicals, Japan). For tdM analysis, the sample was filtered through a 0.45 µm pore size Millex syringe filter (Merck Millipore, USA), then introduced to the SPE-100. The Millex syringe filters were pre-cleaned in order of 1 mol/kg Ultrapur-100 HF (Kanto Chemical, Japan), 1 mol/kg Ultrapur-100 HNO₃ (Kanto Chemical, Japan) and MQW

before drying in a vacuum oven. The 1.0 mol/kg Optima HNO₃ was used for the elution of trace metals. The concentrations of dM and tdM were determined with a high-resolution inductively coupled plasma mass spectrometer (HR-ICP-MS; Element 2, Thermo Fisher Scientific, USA) using a calibration curve method with external standard solutions. The concentration factor of each sample was calculated as the weight ratio of sample solution to eluate.

Procedural blanks were determined using the MQW as a sample. Similar to the process of seawater analysis, MQW was acidified with Optima HCl and then adjusted to pH 6.00 by adding the buffer solution. The detection limits for dM and tdM were defined as three times the standard deviation (SD) of the procedural blank (Table 1). The labile particulate metal (lpM) concentration was calculated as the difference between tdM and dM. The relative standard deviations (RSD) for dM and tdM were approximately 5% at average seawater concentrations for all metals. Therefore, the detection limit (DL) of lpM was defined as twice the propagated uncertainty: $2 \times \sqrt{2} \times 0.05 \times C_{\text{avg}}$, where C_{avg} represents the average concentration of each dM in this study. Values below the DL were classified as not detected (ND). The ND data were assigned a value of $DL \div \sqrt{2}$ for figure preparation except lpPb (Croghan and Egeghy 2003). The values of the procedural blanks, detection limits, C_{avg} and $DL \div \sqrt{2}$ for Al, Mn, Fe, Co, and Pb are listed in Table 1. Certified reference materials of seawater for trace metals (CASS-6 and NASS-7; National Research Council Canada) and GEOTRACES open-ocean reference samples (D2) were measured to confirm the accuracy of our data. The consensus and measured values in this study for Al, Mn, Fe, Co, and Pb are summarised in Supplementary Table 1. Except for Co, our measured values were within 2SD of the consensus values. We abstained from applying UV irradiation in order to minimise contamination risk and avoid unknown effects on the determination of the nine elements (Wuttig et al. 2019; Zheng et al. 2017). Here, we define the dCo data in this study as “non-UV-irradiated dCo”. For simplicity, “non-UV-irradiated dCo” is abbreviated as “dCo” in this paper, except in Sect. 4.1. The results for Ni, Cu, Zn, and Cd will be reported in a forthcoming paper.

3 Results

3.1 Hydrography

The North Pacific Subpolar Gyre (NPSPG) in the study area is formed by the Oyashio, North Pacific Current, Alaskan Current, and Alaskan Stream (Fig. 1). South of the NPSPG, the extension of the Kuroshio Current forms a southern part of the North Pacific Current at approximately 40° N. The North Pacific Current splits as it approaches North

Table 1 Procedural blank and detection limit

Element	Unit	Fraction	Procedural blank		Detection limit	DL $\div \sqrt{2}$	C_{avg}
			n	Average \pm SD			
Al	nmol/kg	td	46	0.13 \pm 0.12	0.36	0.26	0.41
		d	24	0.031 \pm 0.029	0.088	0.06	
		lp	–	–	0.058	0.04	
Mn	nmol/kg	td	46	0.0021 \pm 0.004	0.013	0.01	0.79
		d	24	0.0010 \pm 0.001	0.003	0.00	
		lp	–	–	0.11	0.08	
Fe	nmol/kg	td	46	0.045 \pm 0.069	0.21	0.15	0.71
		d	24	0.041 \pm 0.025	0.076	0.05	
		lp	–	–	0.10	0.07	
Co	pmol/kg	td	46	0.3 \pm 0.6	1.9	1.3	33.5
		d	24	0.3 \pm 0.3	0.8	0.57	
		lp	–	–	4.7	3.4	
Pb	pmol/kg	td	46	0.4 \pm 0.3	0.8	0.59	26.6
		d	24	0.2 \pm 0.1	0.4	0.31	
		lp	–	–	3.8	2.7	

America, and part of it flows anticlockwise to join the Alaskan Current.

The full-depth sectional distributions of potential temperature and salinity along 47° N and 145° W are shown in Supplementary Fig. 1. The water masses identified in the study area are Okhotsk Sea Mode Water (OSMW), NPIW, Dichothermal Water (DtW), Pacific Deep Water (PDW), and Lower Circumpolar Deep Water (LCDW) (Talley et al. 2011). The OSMW with a potential density anomaly (σ_θ) of 26.6–27.0 kg/m³ flows from the Okhotsk Sea and spreads southeast, forming the NPIW around station CL-1. The NPIW is identified with a salinity of 33.8 and 26.7–27.2 σ_θ with a depth range of 200–1000 m, spreading over the sub-polar gyre. The DtW, characterised by a potential temperature minimum, was found at depths of 100–150 m at stations CL-1 to CL-3. The PDW and LCDW were characterized in ranges of 27.7–27.8 σ_θ and 27.8–27.9 σ_θ , respectively. The PDW is formed from the upwelling and diffusion of the LCDW. The LCDW is found just above the bottom of the subarctic Pacific Ocean and is characterised by salinity greater than 34.7, flowing eastward at the north of 40° N.

3.2 Full-depth sectional distribution

3.2.1 47° N zonal transect

The seawater data are summarised in Supplementary Table 2. The full-depth sectional distributions of dM and lpM along the 47°N transect are shown in Fig. 2. dAl reached maxima above the bottom (Fig. 2a). The dAl concentration was relatively high at station CL-1 from the surface to the bottom, with the highest value of 1.79 nmol/kg at a depth of 99 m. lpAl also showed maxima near the bottom over

the transect (Fig. 2f). At station CL-1, there were slightly higher lpAl concentrations from the surface to a depth of 2000 m. The concentrations of dAl and lpAl were low in PDW between 160° W and 145° W.

The maxima of dMn were generally observed in surface water (Fig. 2b), with especially high concentration observed at station CL-1. At this station, the lpMn concentration in the surface water was also high (Fig. 2g). For depths of 1500–2000 m and approximately 3000 m at station CL-21 above the Juan de Fuca Ridge, the dMn and lpMn concentrations were exceptionally high (dMn: 1.86–5.56 nmol/kg; lpMn: 0.30–4.39 nmol/kg).

Both dFe and lpFe were depleted in surface water over the transect (Fig. 2c, h). The dFe concentrations in intermediate and deep waters were generally higher at western than eastern stations. However, the highest concentration of dFe (2.41 nmol/kg) was observed at a depth of 1500–2000 m at the easternmost station, CL-21. Below 1500 m at this station, lpFe concentration increased to 2.59–8.82 nmol/kg (Fig. 2h). The highest concentrations of lpFe (19.2–19.8 nmol/kg) were observed above the bottom at stations CL-17 and CL-19 concurrently with lpAl.

The dCo concentration reached its maximum in subsurface water with \sim 26.0 σ_θ and then gradually decreased with depth (Fig. 2d). The lpCo concentration was slightly higher in subsurface water at some stations and reached its highest values above the bottom (Fig. 2i). At 2500–3000 m depths, dCo concentration was lower (13.4–15.1 pmol/kg) at station CL-21 than at neighbouring stations. In contrast, a lpCo maximum was observed at 3000 m depth at station CL-21.

Maximum dPb concentrations were at depths of 150–400 m with \sim 27.0 σ_θ (Fig. 2e). Within this depth range, the dPb concentration between 150°W and 130°W

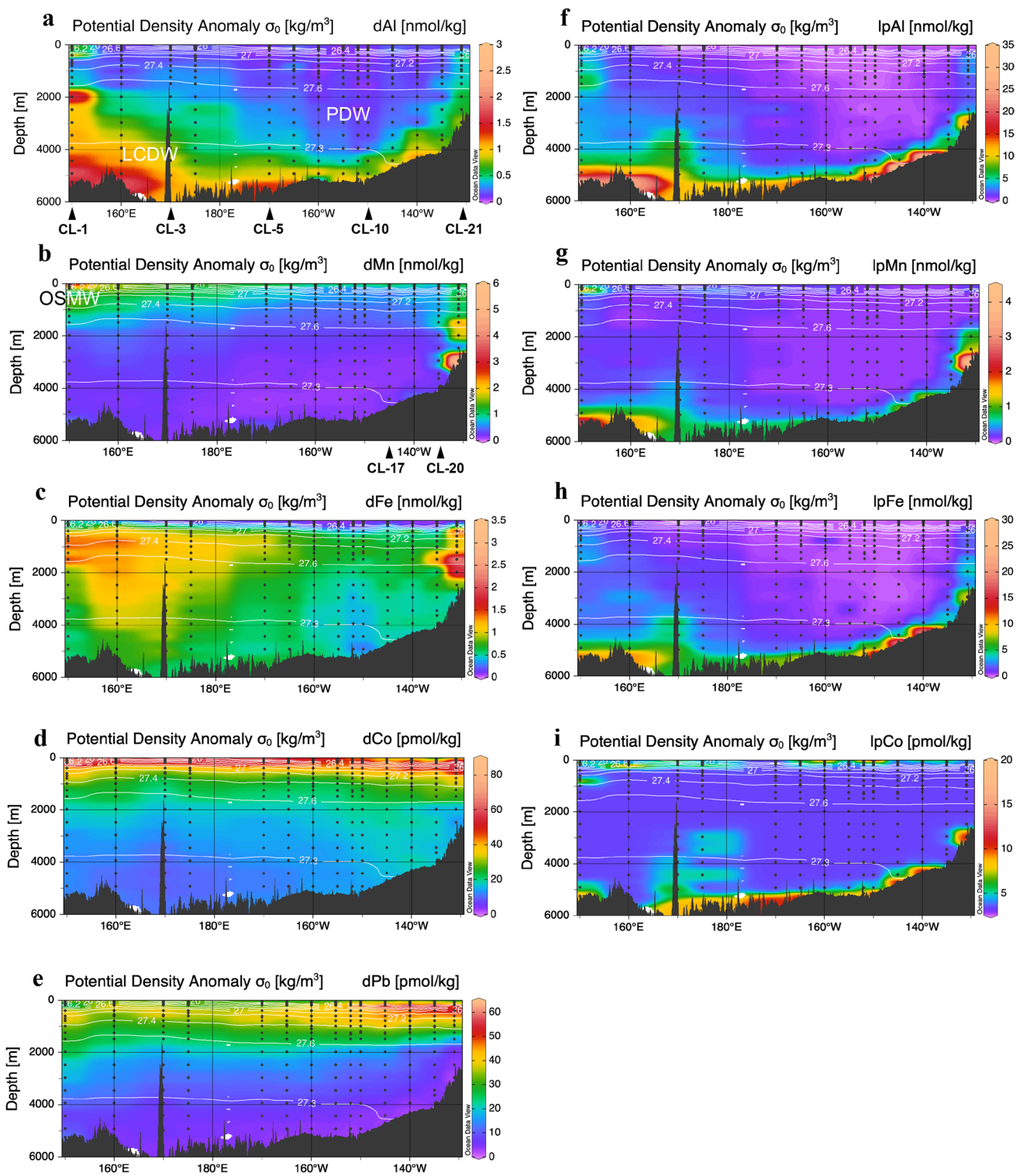


Fig. 2 Full-depth sectional distributions of **a–e** dM and **f–i** lpM along 47° N zonal transect. *LCDW* lower circumpolar deep water, *OSMW* Okhotsk sea mode water, *PDW* Pacific deep water

was higher than that at the other stations. At station CL-21, the dPb concentration below 1500 m depth was lower (2.4–5.1 pmol/kg) than that at the neighbouring stations.

3.2.2 145° W meridional transect

The full-depth sectional distributions of dM and lpM along

the 145°W transect are shown in Fig. 3. Both dAl and lpAl showed maxima above the bottom (Fig. 3a, f), as well as the 47°N transect. From the surface to 1000 m depth at stations between CL-12 and CL-14, extremely high concentrations

of dAl and lpAl were detected (dAl up to 5.6 nmol/kg; lpAl up to 381 nmol/kg).

The maxima of dMn concentration appeared in surface water (Fig. 3b), whereas the lpMn maxima were found

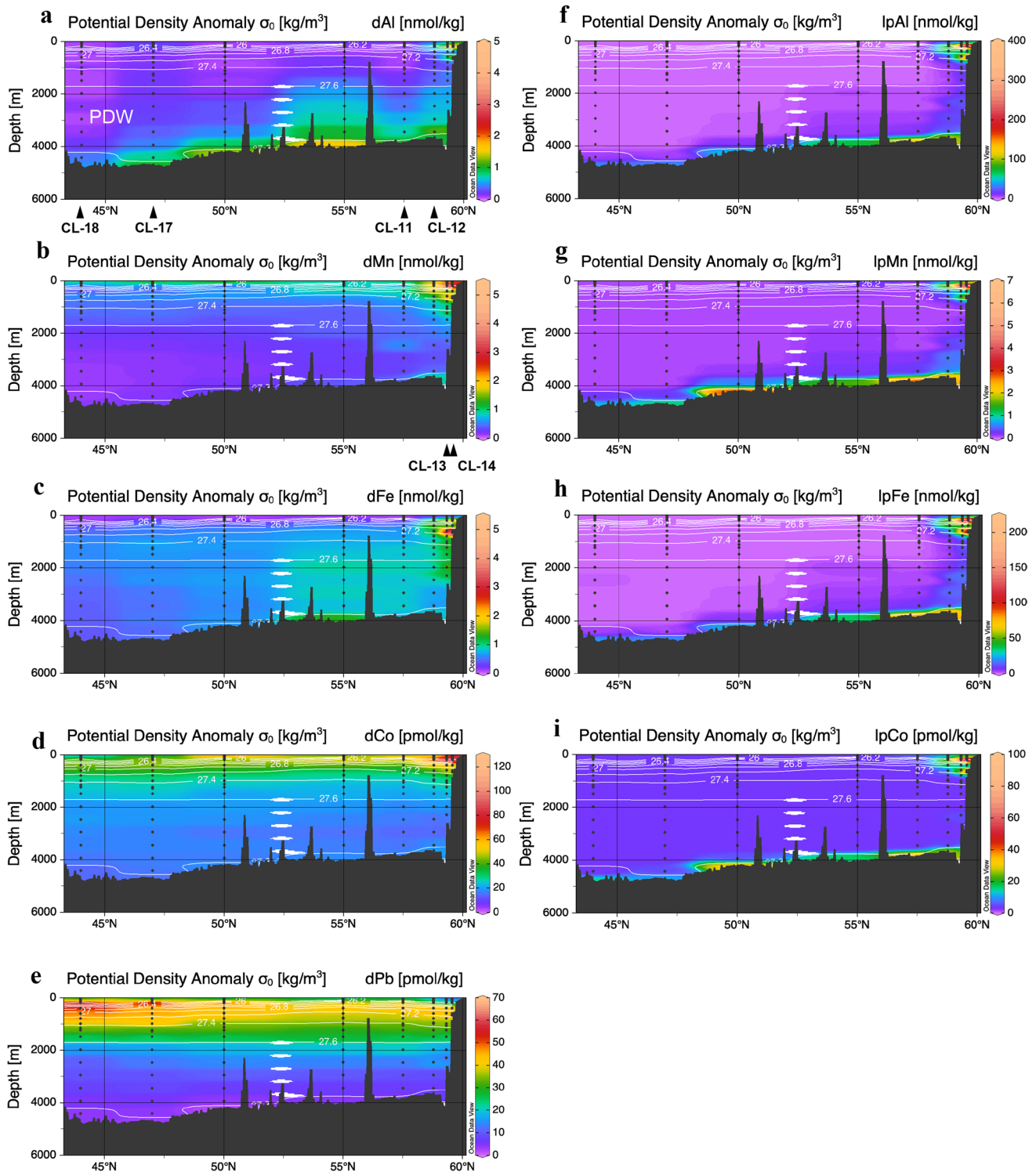


Fig. 3 Full-depth sectional distributions of **a–e** dM and **f–i** lpM along 145° W meridional transect. *PDW* Pacific deep water

above the bottom (Fig. 3g). High concentrations of dMn and lpMn were detected from the surface to a depth of 1000 m at stations between CL-12 and CL-14, concurrently with those of dAl and lpAl.

dFe and lpFe were depleted in surface water (Fig. 3c, h), as well as the 47° N transect. Above a depth of 1000 m, at stations between CL-12 and CL-14, dFe showed maxima similar to those of dAl and dMn. However, only dFe showed slightly higher concentrations in intermediate and deep waters at stations north of 55°N. In contrast, the distribution of lpFe was similar to that of lpAl (Fig. 3h). The subsurface lpFe concentration at station CL-14 was elevated to an exceptional maximum of 211 nmol/kg.

dCo showed maxima within the depth range 0–1000 m at stations between CL-12 and CL-14 (Fig. 3d). dCo also showed maxima in subsurface water with ~26.0 σ_θ throughout the transect. The distribution of lpCo resembled that of lpMn (Fig. 3i). The lpCo concentration was uniformly low from the surface to a depth of 3500 m between 44° N and 55° N.

The dPb maxima occurred within the depth range 150–400 m throughout the transect (Fig. 3e). In contrast to

the other dMs, the highest concentration of dPb (64 pmol/kg) was observed at station CL-18.

3.2.3 lpPb

Because lpPb was not detected in 89% of all data, the sectional distributions of lpPb along both transects are not shown. However, lpPb was detected in subsurface and bottom waters at station CL-1, in surface to subsurface waters at stations CL-7 and CL-15, in subsurface water at stations CL-12 and CL-13, and in subsurface to bottom waters at station CL-14. Between stations CL-12 and CL-14, lpPb maxima occurred at 150 m depth, and the highest value was observed at station CL-13 (19.7 pmol/kg).

3.3 Horizontal distribution

The horizontal distributions of dM at a depth of 10 m, which is the shallowest sampling depth and within the surface mixed layer at stations in this study, are shown in Fig. 4a–e. The dAl concentration in surface water was high off the coast of Alaska (Fig. 4a). The dAl concentration in surface water at other stations was generally low, except for station

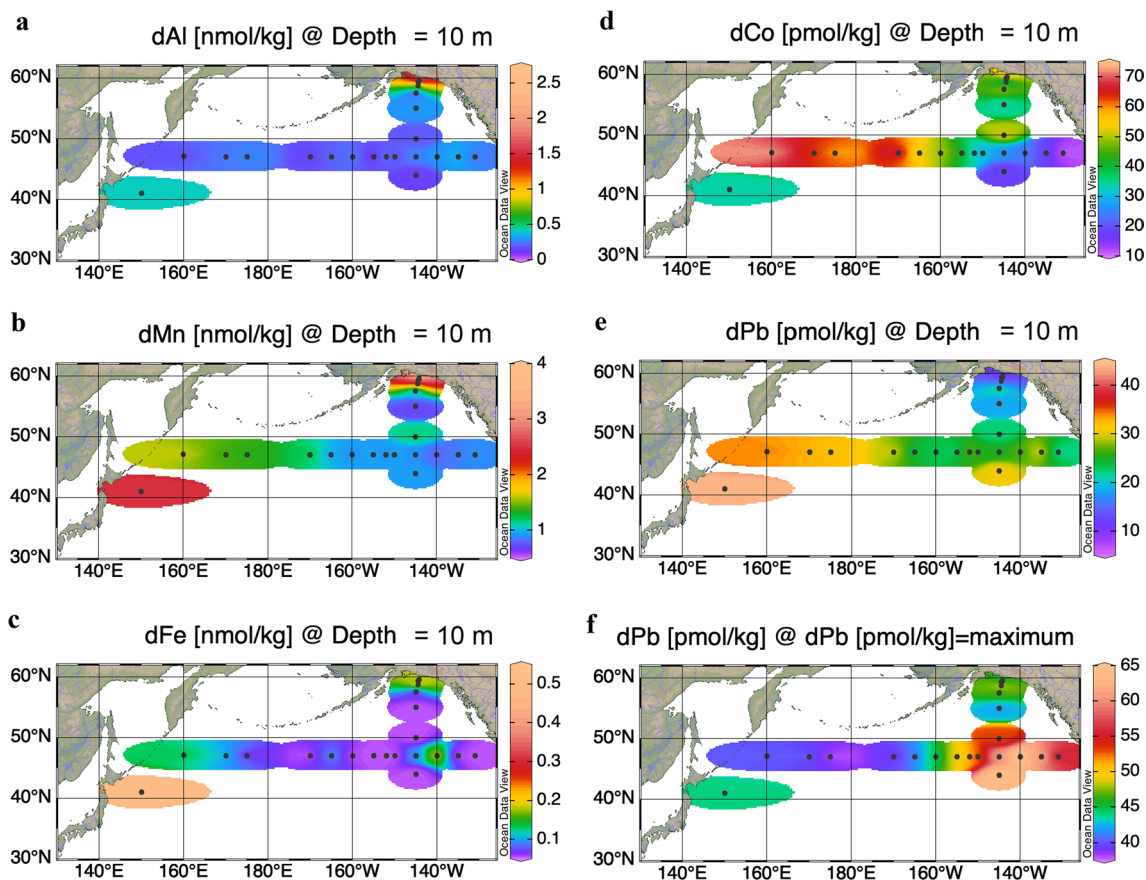


Fig. 4 a–e Horizontal distributions of dM at 10 m depth. f Horizontal distribution of dPb at the depth of dPb maximum

CL-1. The dMn concentration in surface water showed an eastward-decreasing trend along the 47° N transect, and a high concentration was observed off Alaska in a manner similar to that of dAl (Fig. 4a, b). dFe generally showed very low surface concentration, but increased to about 0.15 nmol/kg at stations CL-2 and CL-19, and stations off Alaska at CL-12 to CL-14 (Fig. 4c). The dCo concentration in surface water fluctuated within the range 33.7–72.8 pmol/kg between 150° E and 170° W, which was higher than that at stations east of 160° W (Fig. 4d). dCo was generally higher at northern stations CL-12 to CL-14 along the 145° W transect in the Gulf of Alaska. The dPb concentration in surface water was also higher at the western stations CL-1 to CL-4 along the 47° N transect (Fig. 4e). However, the higher dPb values within the Pb maxima at the depth of 150–400 m were observed at the western stations rather than the eastern stations (Fig. 4f).

4 Discussions

4.1 Study of methodology and sample storage based on comparison with the historical data set

This study is the first to report the distributions of the td and lp fractions of Al, Mn, Fe, Co, and Pb during the KH-17-3 cruise. Other researchers have independently determined dMn and dFe in seawater samples from the KH-17-3 cruise (Nishioka et al. 2020; Wong et al. 2022). Herein, we compare our dMn and dFe data with theirs. Our dMn and dFe values are plotted against literature data in Supplementary Figs. 2a and 2b, respectively. The analytical procedure used by Wong et al. (2022) was quite similar to ours; they used Nobias Chelate-PA1 resin for preconcentration and HR-ICP-MS for quantification. Our dMn data show strong linearity ($R^2=0.97$, $n=357$) against the data by Wong et al. (2022) with a slope of approximately 1.14 (Supplementary Fig. 2a). The ratio of $dMn_{\text{this study}}/dMn_{\text{Wong}}$ for each sample is 1.18 ± 0.18 (avg \pm sd, $n=357$). Thus, both data are basically consistent, but there is a systematic error between them. However, because the vertical profiles of $dMn_{\text{this study}}$ at revisited stations (CL-3 and CL-5) are consistent with those in our previous study (Zheng et al. 2019) (Supplementary Fig. 3), our dataset is highly reproducible. Our dFe data show a strong linearity ($R^2=0.87$, $n=363$) against the data of Nishioka et al. (2020) with a slope of approximately 1.06 after removing two outliers (Supplementary Fig. 2b). Thus, we also consider that the two data sets of dFe are consistent within an analytical error. The two outliers were obtained above the bottom at station CL-14, where the tdFe concentration was extremely high (121–154 nmol/kg). Nishioka et al. (2020)

utilised flow-injection analysis with chemiluminescence detection of dFe at pH 3.2. They analysed their samples onboard or onshore with a storage time of 24 h to 3 months at pH < 2. Our dM samples were acidified to a pH of ~ 1.9 and stored for at least 2 years prior to analysis. It has been reported that dM is stabilised by ligands (Madison et al. 2013) and that some portions of metal-binding ligands and colloidal metal species reside in a colloidal size range of 0.02–0.4 μm , especially for dFe (Boyd and Ellwood 2010; Wu et al. 2001). These metal species may be undetermined when the storage time is short. It is possible that our longer storage time dissociated Fe from the complexes and colloids more effectively, resulting in higher concentrations of dFe.

We compared our non-UV-irradiated dCo data at station CL-9 with those at station 8 from the GEOTRACES GP15 expedition conducted in 2018 (Chmiel et al. 2022). As both stations were located at 47° N, 152° W, approximately 900 km from the continental shelf of Alaska, they are considered crossover stations. The vertical distributions of dCo are compared in Supplementary Fig. 4. Chmiel et al. (2022) determined the concentrations of dCo and “labile dCo” onboard or onshore using cathodic stripping voltammetry (CSV) with dimethylglyoxime (DMG). Seawater samples were filtered through a filter with a 0.2 μm pore-size, but not acidified. Prior to the determination of dCo, the filtered seawater samples were irradiated with UV for 1 h in acid-washed quartz tubes. For the determination of labile dCo, the filtered seawater samples without UV irradiation were allowed to equilibrate with DMG for a long time (8 h) prior to the CSV analysis. The dCo concentration at station 8 is generally higher than our dCo concentration at station CL-9 (Supplementary Fig. 4b), which may be due to the effect of UV irradiation. It is widely assumed that UV irradiation dissociates natural ligand-Co complexes, allowing more dCo species to be detected. On the other hand, the labile dCo concentration at station 8 is generally lower than our dCo concentration at station CL-9 (Supplementary Fig. 4c). Chmiel et al. (2022) suggested that ICP-MS measurements give consistently different results than their electrochemical method and that this may be due to the different kinetics of Co complex formation between DMG and the chelating resins. These results indicate that the difference in methodology results in systematic errors in the dCo concentration. However, it should be noted that our non-UV-irradiated dCo by ICPMS shows a less fluctuated vertical profile than dCo and labile dCo by the electrochemical method. In addition, because the vertical profiles of non-UV-irradiated dCo at revisited stations (CL-3 and CL-5) are consistent with those in our previous study (Zheng et al. 2019) (Supplementary Fig. 5), we think non-UV-irradiated dCo is useful enough to consider the profile as a relative value.

4.2 Evaluation of the scavenging process by labile particle metals

The lpM/tdM ratio was 0.79 ± 0.16 ($n = 290$) for Al, 0.35 ± 0.22 ($n = 213$) for Mn, and 0.56 ± 0.25 ($n = 326$) for Fe. With a moderate proportion exists in seawater, particulate species are also essential components for the biogeochemical cycling of these metals. dMn and dCo had the highest correlation coefficient of 0.65 ($n = 422$) among dM pairs. However, the correlation coefficient was higher than 0.78 for all lpM pairs. The strongest correlation was observed between the lpAl and lpFe concentrations. lpFe and lpAl showed strong linearity ($R^2 = 0.98$, $n = 266$) in the subarctic Pacific Ocean (Fig. 5a). The slope of the lpFe vs. lpAl regression line was 0.637, which is of the same order of magnitude as the average Fe/Al ratio of 0.33 in the Earth's crust (Taylor 1964). As mentioned in the Results section, high concentrations of lpAl and lpFe were mainly observed in surface to subsurface waters near the continent and in bottom water. The resuspension of sediments releases lpAl and lpFe into bottom waters. The higher lpFe/lpAl ratio in the subarctic Pacific Ocean relative to the ratio of Earth's crust may be due to the biological uptake of dFe by phytoplankton in surface water and the preferential scavenging of dFe throughout the water column (Zheng and Sohrin 2019).

lpCo was found to have correlation coefficients of 0.97 ($n = 68$) with lpAl, 0.86 ($n = 84$) with lpMn, and 0.96 ($n = 63$) with lpFe. lpCo and lpMn exhibited a linear correlation of $R^2 = 0.75$ ($n = 84$; Fig. 5b). A unique feature of lpMn and lpCo is that the lpM/tdM ratio generally increased with depth. Because lpMn and lpCo were mainly detected above the continental slope and in bottom water, the correlation may reflect the co-release of dMn and dCo from anoxic sediments by Mn reduction (Cid et al. 2011). In oxic water,

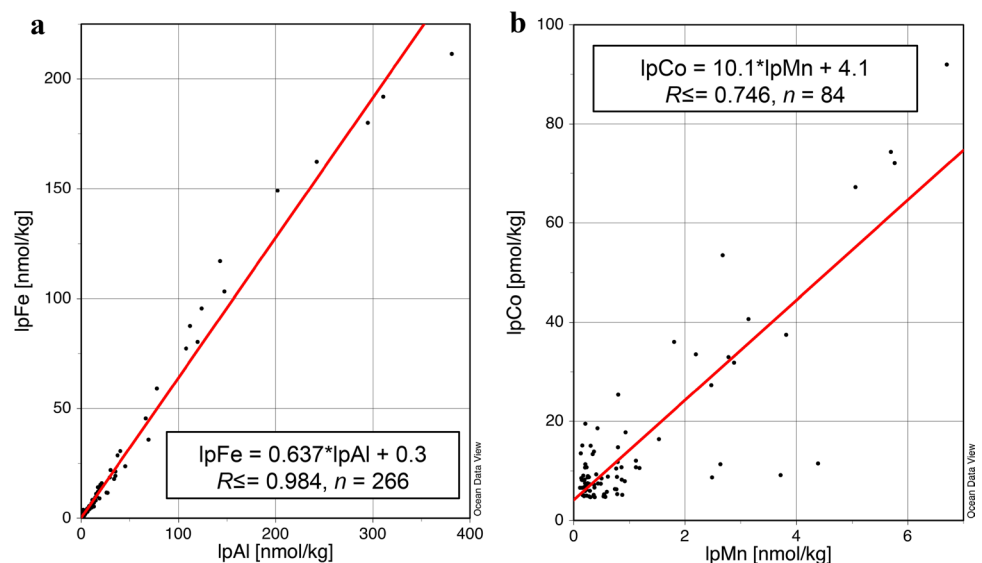
dCo is co-oxidised with dMn via the common microbially catalysed pathway (Moffett and Ho 1996). The supply of dMn and dCo to shallow water, and the oxidising scavenging throughout the water column are major causes for the increasing lpM/tdM ratio with depth.

High concentrations of lpMn and lpFe were observed at 2000 m depth at station CL-21 (Fig. 2g, h), where dMn and dFe were also high (Fig. 2b, c). There are many reports on hydrothermal activity around the Juan de Fuca Ridge (Butterfield et al. 1994). Station CL-21 was located about 30 km from the Cobb Seamount ($46^\circ 44' 0''$ N, $130^\circ 47' 0''$ W) and about 140 km from the active Axial Seamount ($46^\circ 03' 36''$ N, $130^\circ 00' 0''$ W) that is at the terminal of the Cobb–Eickelberg Seamount chain (Chadwick et al. 2014; Desonie and Duncan 1990). Previous research reported elevated concentrations of lpAl, lpMn, and lpFe in deep water near station CL-21, which were attributed to the effects of hydrothermal plumes (Zheng et al. 2017). The lpCo maximum observed in this study is likely due to the scavenging of dCo by Fe–Mn oxyhydroxide particles in the hydrothermal plumes (Noble et al. 2017), because a concurrent decrease in dCo was detected (Fig. 2d). Although lpPb was not detected at CL-21, the slightly low dPb concentration (Fig. 2e) may also be due to scavenging by Fe–Mn oxyhydroxides in hydrothermal plumes (German et al. 1991).

4.3 Boundary scavenging in the Gulf of Alaska

In a previous study by Zheng and Sohrin (2019), the integral concentrations of tdM and dM at each station decreased exponentially within a distance of approximately 500 km along 160° W from the continental shelf break of the Aleutian Islands, indicating that boundary scavenging occurred within this zone. In this study, we evaluate boundary

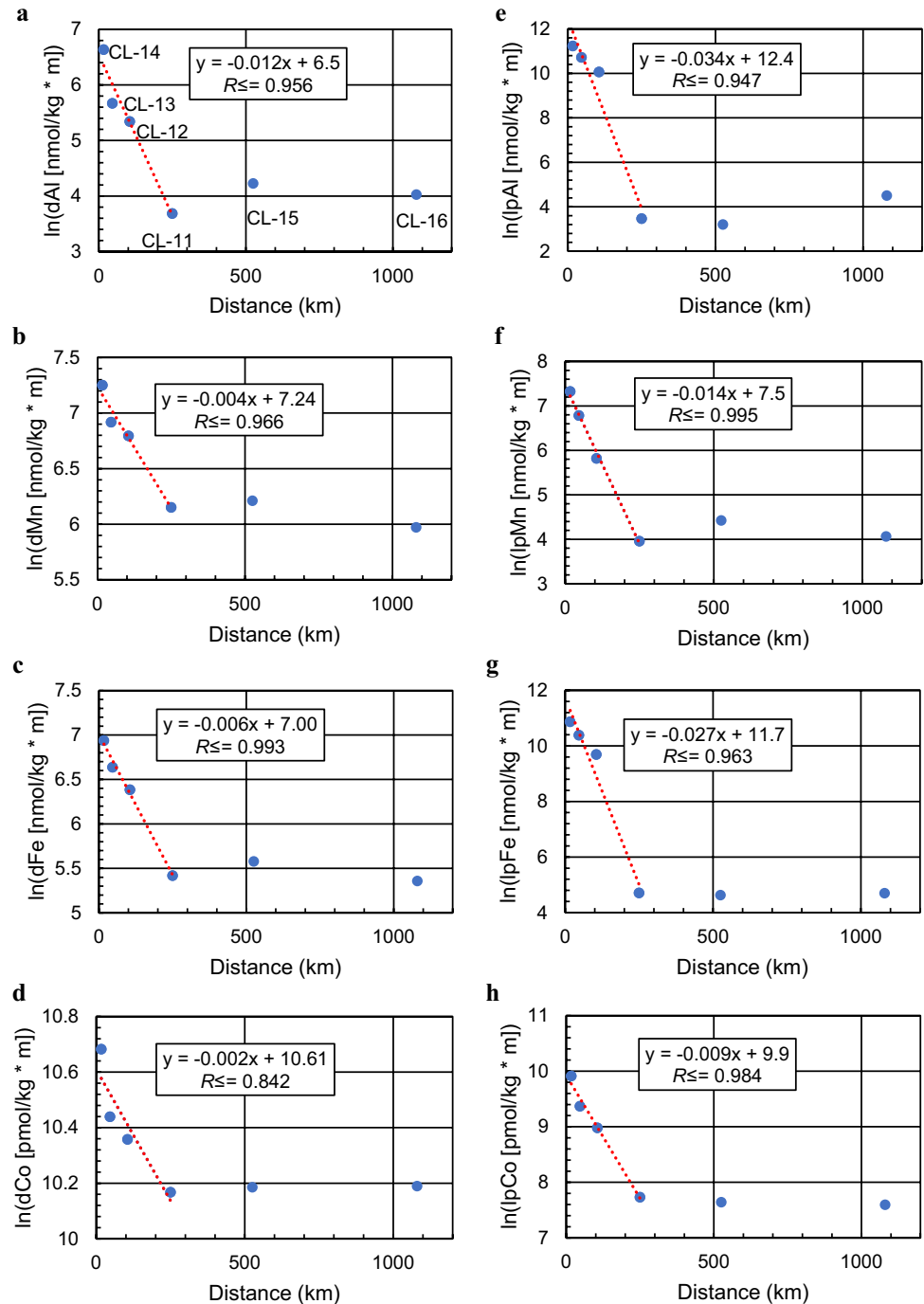
Fig. 5 a lpFe vs. lpAl. b lpCo vs. lpMn. Regression lines are indicated in red (color figure online)



scavenging in the Gulf of Alaska using concentrations of dissolved and labile particulate Al, Mn, Fe, and Co along the 145° W transect. Because the bottom depth was 695 m at the shallowest station CL-14, we calculated integral concentrations of dM and lpM from the surface to a depth of 600 m ($\sim 27.20 \sigma_\theta$) at each station. The natural logarithm of integral concentrations of dM and lpM from stations CL-11 to CL-16 are plotted against the distance from the continental shelf break (59° 42' 7.6" N, 144° 6' 15.7" W, 200 m depth) in Fig. 6. All d and lp species of Al, Mn, Fe, and Co showed

linear decreasing trends ($R^2 = 0.84\text{--}0.99$) from the shelf break to about 250 km offshore. Beyond 250 km, the integral concentrations of dM and lpM levelled off. The integral concentration of lpAl was a few orders of magnitude higher than dAl from the shelf edge to approximately 100 km offshore, then levelled off to a similar value (Fig. 6a, e). In contrast, integral concentrations of dMn and lpMn were comparable within a 100 km distance, but lpMn levelled off to a lower offshore value (Fig. 6b, f). dFe and lpFe exhibited trends similar to those of dAl and lpAl, respectively. Although lpFe

Fig. 6 Natural logarithm of integral concentrations of **a–d** dM and **e–h** lpM from the surface to 600 m depth at stations CL-11 to CL-16, plotted against the distance from the continental shelf edge. Red dotted lines represent regression lines for stations CL-11 to CL-14 (color figure online)



was higher than dFe near the continent, their levelling-off values were similar (Fig. 6c, g). The decrements of dCo and lpCo off Alaska were the smallest among dMs and lpMs, respectively (Fig. 6d, h). In contrast, the integral concentration of dPb did not significantly decrease with increasing distance from the shelf-break. These decreasing trends of dM and lpM species cannot be explained by water mass mixing, because temperature and salinity are uniform in this zone (Supplementary Figs. 1c and 1d). From these decreasing trends, we estimated that the boundary scavenging zone is approximately 250 km wide in the Gulf of Alaska. Boundary scavenging causes significant effects on Al, Mn, Fe, and Co, but not on Pb. The explanation for Pb will be given in Sect. 4.5 in detail.

Previous study of our laboratory indicated that the width of the boundary scavenging zone is ~ 500 km along 160° W off the Aleutian Islands (Zheng and Sohrin 2019). Compared with ~ 250 km along 145° W off Alaska, the shorter distance in the Gulf of Alaska may be due to stronger scavenging caused by higher particulate inputs from rivers. The maximum lpAl concentration at station CL-14 was 381 nmol/kg, which is approximately seven times higher than that at stations near the Aleutian Islands. The northern end of the 145° W transect is close to the Copper River and Bering River estuaries, which originate from glacial runoffs. Brown et al. (2010) reported that scavenging of trace metals on the continental shelf off Alaska is highly active by enormous particulate inputs from rivers. dAl and lpAl in surface water decreased with salinity. They suggested that the average residence time of dAl in the shelf waters of the northern Gulf of Alaska was approximately 10 days. Michael et al. (2023) reported that glacial meltwater is the major source of tdAl and tdMn in the coastal Gulf of Alaska during summer. From the results of the GEOTRACES GP15 expedition, Chmiel et al. (2022) found high concentrations of dCo and particulate Co in surface to subsurface waters and pointed out the fresh riverine input and sedimentary particle flux of Co. They indicated that Co released at the coast entered the Alaskan Stream, and that elevated dCo concentrations were not observed beyond the Stream. Those results are consistent with the present study.

4.4 East–west gradients in dM and lpM

In the subarctic Pacific, there are east–west differences in phytoplankton communities (Suzuki et al. 2002). The subarctic Pacific is one of the HNLC regions, whereas the western subarctic Pacific is more productive than the eastern Pacific, particularly during the bloom season from late spring to early summer. The photosynthetic activity of phytoplankton shows a decreasing trend from west to east (Suzuki et al. 2002). It has been suggested that these differences are controlled by the supply of dFe. dFe is mainly

supplied from the Asian Continent to the subarctic Pacific Ocean via aeolian dust transport and ocean circulation, resulting in east–west gradients in the flux and distribution of Fe in seawater (Nishioka et al. 2021). This was confirmed in the present study. The horizontal distributions of dM in surface water show apparent east–west gradients (Fig. 4).

In this study, we investigated the isopycnal transport of dM and lpM in the subarctic Pacific. We selected the isopycnal surface of 25.90 σ_θ , which is generally below the surface mixed layer with a depth of ~ 30 m in the west and ~ 120 m in the east. Data from the Bering Sea (Cid et al. 2011), the Japan and Okhotsk Seas (Nakaguchi et al. 2022), and the Pacific (Zheng et al. 2019) are combined in Fig. 7. In general, Al, Mn, Fe, and Co show similar distributions. The highest concentrations of dM and lpM were found in the Bering Sea shelf water, except for dPb. Relatively high concentrations of dM spread from the Okhotsk Sea to the western subarctic Pacific. Comparably high concentrations of dM and lpM are also observed along the coast of Alaska. However, the spread of dM and lpM is limited in the eastern subarctic Pacific region. This is attributed to the boundary scavenging described above. Thus, we propose that boundary scavenging is a factor controlling the east–west gradients in dM and lpM in the subarctic Pacific, which also affects the east–west differences in the phytoplankton community. Apparently, dPb has a distinct isopycnal distribution compared with the other metals. The origin of this phenomenon is discussed in detail in the following section.

4.5 Temporal change: dPb in the middle of the subarctic gyre

Combining with previous publications, our laboratory observed the vertical profiles of five elements at 160° W for 13 years. Stations ST-12 and 13 were occupied during KH-05-2 cruise, station BD-15 during KH-12-4 cruise (Zheng et al. 2019), and station CL-7 during KH-17-2 cruise (Fig. 8a). Stations ST-12, 13, and BD-15 are located at about 200–400 km from station CL-7 (47° N, 160° W). The vertical profiles of d and lp of Al, Mn, Fe, and Co generally showed decreasing concentrations with increasing distance from the Aleutian Islands independent of sampling time, indicating that boundary scavenging is the major controlling factor (Supplementary Figs. 6 and 7). In Supplementary Fig. 6e, the vertical profile of phosphate did not show significant variations above 1000 m depth, particularly between ST-13 and BD-15, suggesting minor effects of ocean circulation on the distribution of phosphate. However, the vertical profiles of dPb exhibit a distinct trend (Fig. 8b). The subsurface maximum of dPb at 100–200 m depth was the highest at ST-12. Previous studies reported that dPb had the highest concentration at approximately 35° N and a depth of approximately

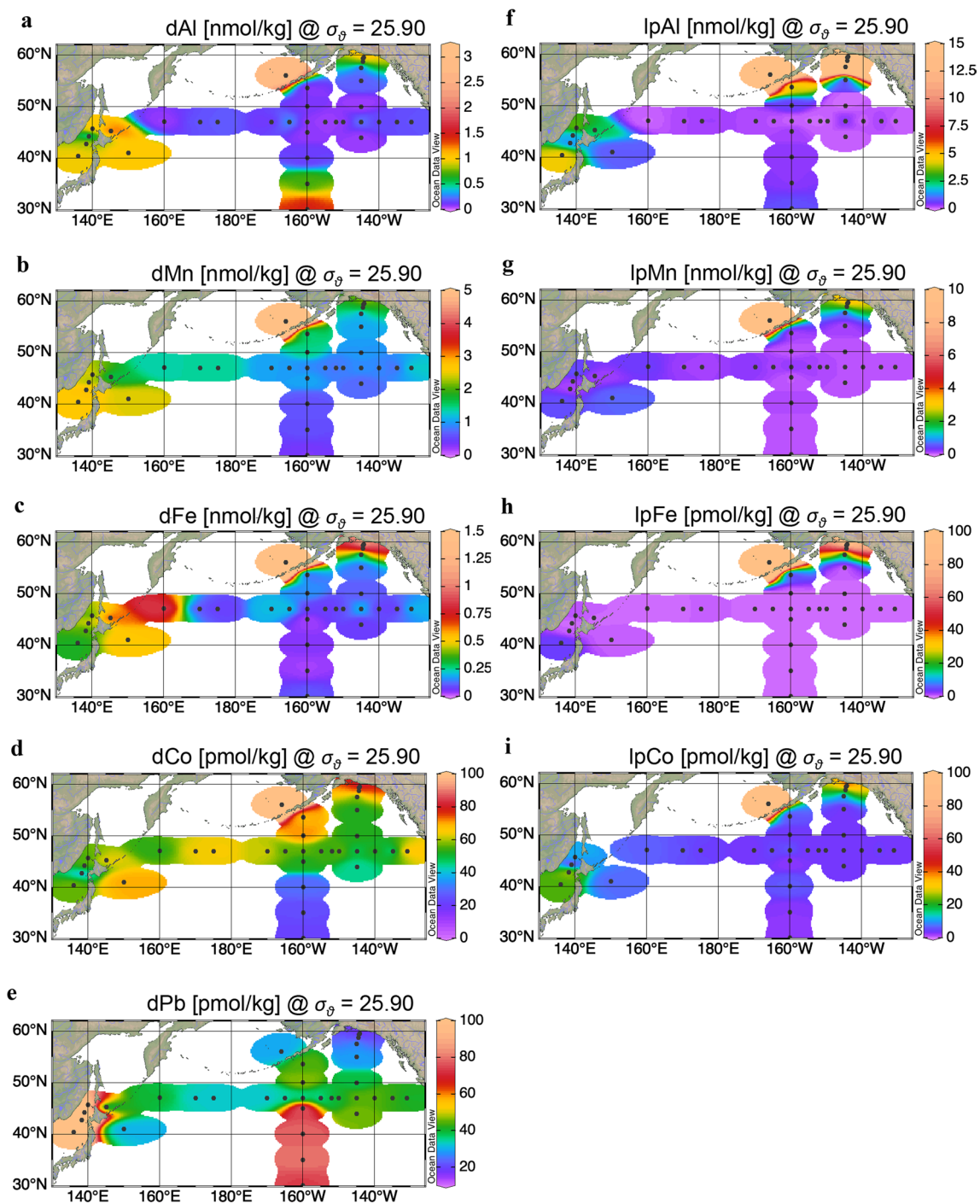


Fig. 7 Distributions of **a–e** dM and **f–i** lpM on an isopycnal surface of $25.90 \sigma_\theta$. Data for the Bering Sea, the Sea of Japan and Okhotsk, and along 160° W were adopted from Cid et al. (2011), Nakaguchi et al. (2022), and Zheng et al. (2019), respectively

200 m in the North Pacific and that the dPb/dAl ratio in the North Pacific is substantially higher than the Pb/Al ratio in upper crust (Zheng et al. 2019, 2022). The distribution is explained by the following mechanism: Pb is predominantly supplied as anthropogenic aerosols via westerlies centred at approximately 35° N. The enormous atmospheric

input of Pb into the North Pacific Ocean originates from Asian countries and Russia, as evidenced by isotopic analysis of Pb (Zurbrick et al. 2017). Sources of anthropogenic Pb aerosols include leaded gasoline, coal combustion, metal smelting, cement production, and municipal solid waste incineration (Li et al. 2012; Zurbrick et al. 2017).

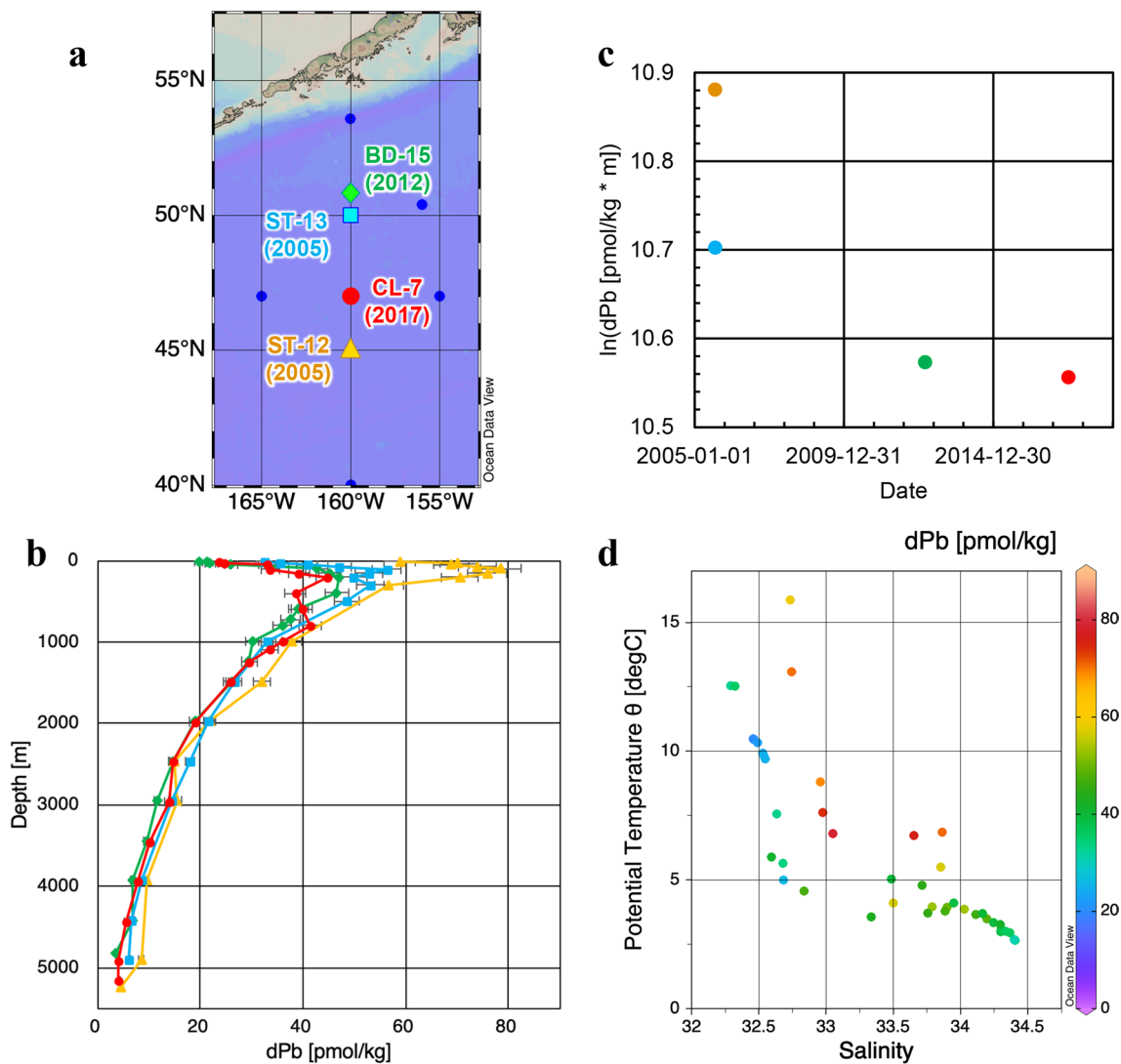


Fig. 8 **a** Map showing stations along 160° W chosen for comparison of dPb. ST-12 and ST-13 are stations of the 2005 KH-05-2 cruise. BD-15 is a station of the 2012 KH-12-4 cruise. Data from the KH-05-2 and KH-12-4 cruises were adopted from Zheng et al. (2019). **b** Comparison of vertical dPb profiles at stations ST-12 (yellow triangles), ST-13 (blue squares), BD-15 (green diamonds), and

CL-7 (red dots). Error bars represent 1 SD. **c** Natural logarithm of integral concentration of dPb from the surface to 1000 m depth at stations ST-12, ST-13, BD-15, and CL-7, plotted against the sampling date. **d** Temperature–salinity diagram of stations ST-12, ST-13, BD-15, and CL-7 from the surface to 1000 m depth, colour indicates dPb concentration (color figure online)

dPb is released from the aerosols, enters the Subtropical Mode Water and Central Mode Water (CMW) during winter convection, and is transported with the mode water. The highest value observed at ST-12 was partly explained by this station's close proximity to the formation area of CMW (36°–43° N, 150° E–160° W; Yasuda and Kitamura (2003)). Examining the temperature–salinity diagram above a depth of 1000 m (Fig. 8d), ST-13, BD-15, and CL-7 showed similar water mass structure, while ST-12 showed a different characteristic. Thus, it is possible that the high concentrations (> 60 pmol/kg) of dPb may have been attributed to a higher contribution of CMW at ST-12. However, the trends at the other three stations could not

be explained by a spatial effect; we therefore propose that a temporal effect is important.

We have integrated the dPb concentration from the surface to 1000 m depth in the water column to evaluate the amount of dPb in the upper water. The natural logarithm of the integral dPb concentration was plotted against the sampling date (Fig. 8c). The integral value shows a decreasing trend over time, suggesting that the anthropogenic input of dPb decreased between 2005 and 2017. Although emissions from leaded gasoline have decreased since the 1990s (Flegal et al. 2013), those from the other processes have increased. In 2017, the dPb concentration in surface water was still higher in the western subarctic gyre than in the eastern

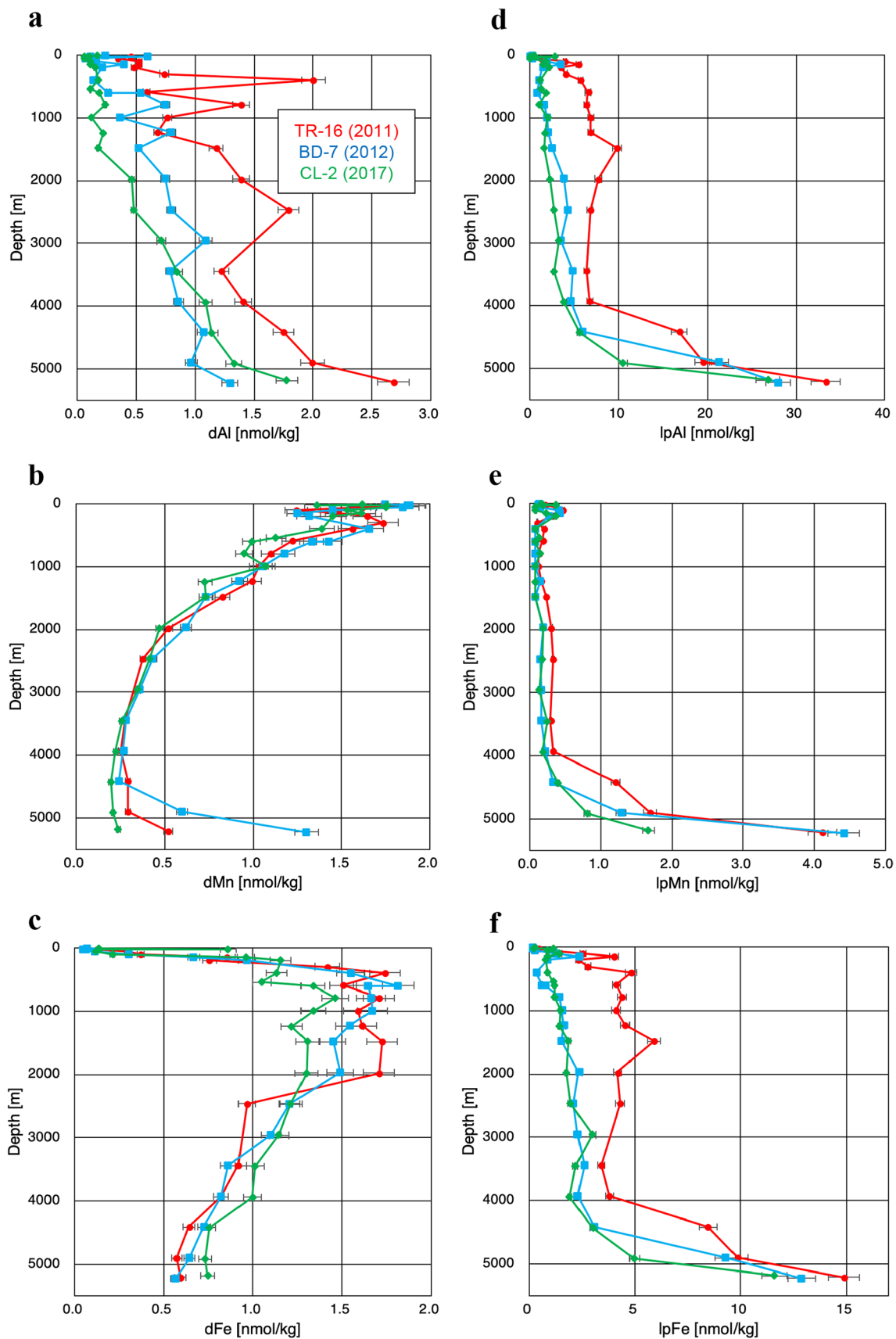


Fig. 9 Comparison of vertical profiles of **a–c** dM and **d–f** lpM at stations TR-16 (red dots), BD-7 (blue squares), and CL-2 (green diamonds). Error bars represent 1 SD. TR-16 is a station of the 2011 KH-11-7 cruise. BD-7 is a station of the 2012 KH-12-4 cruise. Data from the KH-11-7 and KH-12-4 cruises were adopted from Zheng et al. (2019) (color figure online)

subarctic gyre (Fig. 4e), indicating that anthropogenic input of Pb is continuing. Figure 4f shows a general eastward transportation of the subsurface dPb maxima (150–400 m depth). Zurbrick et al. (2017) estimated that the water mass age at the dPb maxima was about 4–12 years. Our finding of decreasing subsurface dPb over time in the middle of the subarctic gyre may reflect the declining use of leaded gasoline.

Lee et al. (2011) reported a decrease in subsurface dPb concentration from 1979 to 2008 in the Sargasso Sea. They suggested that the phase-out of leaded gasoline in America and Europe accounts for the diminishing subsurface dPb maximum. It is probable that the subsurface dPb maximum remains in the North Pacific because the industrial emission of Pb has increased substantially in Asian countries.

4.6 Temporal change: dM and lpM at 47° N, 160° E

Station CL-2 of the KH-17-3 cruise on 27 June 2017, station BD-7 of the KH-12-4 cruise on 28 August 2012 and station TR-16 of the KH-11-7 cruise on 28 July 2011 occupied the same point (47° N, 160° E). These served as crossover stations in the GEOTRACES Program. Here, we compare their results to analyse temporal changes. The data from stations TR-16 and BD-7 were obtained from Zheng et al. (2019). The vertical profiles of dAl, dMn, dFe, lpAl, lpMn, and lpFe exhibit significant temporal changes (Fig. 9). However, dPb and dCo did not show significant temporal changes in deep water, although they showed some temporal variations above a depth of 1000 m (Supplementary Figs. 8a and 8b). In particular, dAl from the subsurface to the bottom decreased from 2011 to 2017 (Fig. 9a). dFe from the subsurface to 2000 m depth decreased with time in a manner similar to that of dAl. lpM in subsurface to deep waters generally decreased, especially for lpAl and lpFe (Fig. 9d, f). To investigate the budget, we integrated the dM and lpM concentrations from the surface to the bottom. The natural logarithm of integral concentration is plotted against the sampling date in Supplementary Fig. 9. dAl, lpAl, lpMn, and lpFe show similar decreasing trends; the integral concentrations decreased by approximately 0.8 orders of magnitude during this period. The integral concentration of dFe decreased slightly throughout the study period (Supplementary Fig. 9c). Although dMn and dCo decreased between 2011 and 2017, slight increases were observed in 2012

(Supplementary Figs. 9b and 9d). lpCo decreased in a manner similar to that of lpMn (Supplementary Figs. 9f and 9h).

Because temporal changes are most apparent in Al and are concurrent with those of some other elements, they may be attributed to an episodic supply of lithogenic materials. We propose that the episodic supply of lithogenic materials resulted from the Great East Japan Earthquake on 11 March 2011 which caused tsunami and submarine effects (Zheng et al. 2019). Earthquakes induce turbidity flows and increase marine sediment suspension, which may in turn transfer organic carbons deposited at shallow depths to deep waters (Thunell et al. 1999). Because the distance between the seismic centre and TR-16 is approximately 1730 km, the effect might have reached TR-16 within three months. The decrease in lpAl, lpMn, lpFe, and lpCo from 2011 to 2017 (Supplementary Figs. 9e–h) could be attributed to continuous scavenging of lithogenic particles supplied by tsunami and ocean circulation. It is likely that this incident also supplied organic matter to the bottom, resulting in temporally anoxic conditions and the release of dMn from the sediments. This may explain the increase in dMn observed in 2012. It seems that the temporal change of these elements is different from that of radiocesium discharged by Fukushima nuclear accident after the earthquake. Kumamoto et al. (2022) observed the temporal distribution of radiocesium in the Pacific, and concluded that radiocesium was remained in the surface layer shallower than 200 m depth approximately until summer 2014 and that the zonal transport speed of the radiocesium plume in the eastern subarctic gyre was about 100 km per month.

5 Conclusions

We report the distribution of the d, td, and lp species of Al, Mn, Fe, Co, and Pb in the subarctic Pacific Ocean during the GEOTRACES Japan KH-17-3 cruise. The td and lp data are reported for the first time and provide a comprehensive view of particulate trace metal distribution in the subarctic Pacific Ocean. This distribution reflects continental sources including fluvial and sediment inputs, particularly in the Gulf of Alaska. At the easternmost station, the effect of the hydrothermal activity of the Juan de Fuca Ridge was observed. The trace metals behaved differently along the north–south and east–west transects of the cruise. The distribution along the north–south transect shows intensive boundary scavenging off the coast of Alaska. We estimated the width of the boundary scavenging zone by analysing the distribution of four scavenged elements (except Pb). Higher fluvial particulate inputs likely resulted in a narrow boundary-scavenging zone. Along the east–west transect, gradients in dM and lpM imply isopycnal transport from the Okhotsk and Bering Seas to the western subarctic Pacific.

In contrast, boundary scavenging limits the spread of the continental supply of metals in the eastern subarctic Pacific. We propose that boundary scavenging is a factor controlling the east–west gradients of trace metals, which in turn affects the phytoplankton community. In addition to spatial effects, we studied temporal changes. Declining anthropogenic emissions of Pb resulted in a decadal change in dPb in the middle of the subarctic gyre. In the western part of the gyre, the Great East Japan Earthquake resulted in elevated concentrations and the subsequent scavenging of trace metals.

Supplementary Information The online version contains supplementary material available at <https://doi.org/10.1007/s10872-023-00710-8>.

Acknowledgements The authors thank the crew, technicians, students, and scientists onboard the KH-17-3 cruise for their assistance with the sampling and analysis of routine data. This research was supported by the Japan Society for the Promotion of Science (JSPS) KAKENHI grants (15H01727 and 19H01148 to YS; 21K17877 to LZ) and by Mitsumasa Ito Memorial Research Grants from the Research Institute for Oceanography Foundation (H31-R1, R2-R2, R4-R7, and R5-R6 to LZ). We would like to thank Editage (<http://www.editage.jp>) for English language editing.

Author contributions YS contributed to the conception and design of this study. Material preparation, data collection, and analyses were performed by C-YC and LZ. The first draft of the manuscript was written by C-YC, and all authors commented on previous versions of the manuscript. All authors read and approved the final manuscript.

Data availability The original data are presented in supplementary material.

Open Access This article is licensed under a Creative Commons Attribution 4.0 International License, which permits use, sharing, adaptation, distribution and reproduction in any medium or format, as long as you give appropriate credit to the original author(s) and the source, provide a link to the Creative Commons licence, and indicate if changes were made. The images or other third party material in this article are included in the article's Creative Commons licence, unless indicated otherwise in a credit line to the material. If material is not included in the article's Creative Commons licence and your intended use is not permitted by statutory regulation or exceeds the permitted use, you will need to obtain permission directly from the copyright holder. To view a copy of this licence, visit <http://creativecommons.org/licenses/by/4.0/>.

References

- Anderson RF, Lao Y, Broecker WS, Trumbore SE, Hofmann HJ, Wolfli W (1990) Boundary scavenging in the Pacific Ocean: a comparison of ^{10}Be and ^{231}Pa . *Earth Planet Sci Lett* 96:287–304. [https://doi.org/10.1016/0012-821X\(90\)90008-L](https://doi.org/10.1016/0012-821X(90)90008-L)
- Bacon MP, Spencer DW, Brewer PG (1976) $^{210}\text{Pb}/^{226}\text{Ra}$ and $^{210}\text{Po}/^{210}\text{Pb}$ disequilibria in seawater and suspended particulate matter. *Earth Planet Sci Lett* 32:277–296. [https://doi.org/10.1016/0012-821X\(76\)90068-6](https://doi.org/10.1016/0012-821X(76)90068-6)
- Balistrieri L, Brewer PG, Murray JW (1981) Scavenging residence times of trace metals and surface chemistry of sinking particles in the deep ocean. *Deep Sea Res Part A Oceanogr Res Pap* 28:101–121. [https://doi.org/10.1016/0198-0149\(81\)90085-6](https://doi.org/10.1016/0198-0149(81)90085-6)
- Boyd PW, Ellwood MJ (2010) The biogeochemical cycle of iron in the ocean. *Nat Geosci* 3:675–682. <https://doi.org/10.1038/ngeo964>
- Brown MT, Lippiatt SM, Bruland KW (2010) Dissolved aluminum, particulate aluminum, and silicic acid in northern Gulf of Alaska coastal waters: Glacial/riverine inputs and extreme reactivity. *Mar Chem* 122:160–175. <https://doi.org/10.1016/j.marchem.2010.04.002>
- Bruland KW, Lohan MC (2003) Controls of trace metals in seawater. In: Holland HD, Turekian KK (eds) *Treatise on geochemistry*. Pergamon, Oxford, pp 23–47
- Butterfield DA, McDuff RE, Franklin J, Wheat CG (1994) Geochemistry of hydrothermal vent fluids from Middle Valley, Juan de Fuca Ridge. *Proc Ocean Drill Progr Sci Res* 139:395–410. <https://doi.org/10.2973/odp.proc.sr.139.266.1994>
- Chadwick J, Keller R, Kamenov G, Yagodzinski G, Lupton J (2014) The Cobb hot spot: HIMU-DMM mixing and melting controlled by a progressively thinning lithospheric lid. *Geochem Geophys Geosyst* 15:3107–3122. <https://doi.org/10.1002/2014gc005334>
- Chester R (2009) *Marine geochemistry*. Wiley, New York
- Chmiel R, Lanning N, Laubach A, Lee J-M, Fitzsimmons J, Hatta M, Jenkins W, Lam P, McIlvin M, Tagliabue A, Saito M (2022) Major processes of the dissolved cobalt cycle in the North and equatorial Pacific Ocean. *Biogeosciences* 19:2365–2395. <https://doi.org/10.5194/bg-19-2365-2022>
- Cid AP, Urushihara S, Minami T, Norisuye K, Sohrin Y (2011) Stoichiometry among bioactive trace metals in seawater on the Bering Sea shelf. *J Oceanogr* 67:747–764. <https://doi.org/10.1007/s10872-011-0070-z>
- Croghan CW, Egeghy PP (2003) Methods of dealing with values below the limit of detection using SAS. *South SAS User Group* 22:24
- Cutter G, Casciotti K, Croot P, Geibert W, Heimbürger L-E, Lohan M, Planquette H, Flierdt Tvd (2017) Sampling and sample-handling protocols for GEOTRACES cruises
- Desonie DL, Duncan RA (1990) The Cobb-Eickelberg Seamount Chain: hotspot volcanism with mid-ocean ridge basalt affinity. *J Geophys Res*. <https://doi.org/10.1029/JB095iB08p12697>
- Flegal AR, Gallon C, Ganguli PM, Conaway CH (2013) All the lead in China. *Crit Rev Environ Sci Technol* 43:1869–1944. <https://doi.org/10.1080/10643389.2012.671738>
- German CR, Von Damm KL (2003) Hydrothermal processes. In: Holland HD, Turekian KK (eds) *Treatise on geochemistry*. Pergamon, Oxford, pp 181–222
- German CR, Campbell AC, Edmond JM (1991) Hydrothermal scavenging at the Mid-Atlantic Ridge: Modification of trace element dissolved fluxes. *Earth Planet Sci Lett* 107:101–114. [https://doi.org/10.1016/0012-821X\(91\)90047-L](https://doi.org/10.1016/0012-821X(91)90047-L)
- Kumamoto Y, Aoyama M, Hamajima Y, Nagai H, Yamagata T, Murata A (2022) Zonal and vertical transports of Fukushima-derived radiocesium in the subarctic gyre of the North Pacific until 2014. *J Environ Radioact* 247:106864. <https://doi.org/10.1016/j.jenvrad.2022.106864>
- Lam PJ, Ohnemus DC, Auro ME (2015a) Size-fractionated major particle composition and concentrations from the US GEOTRACES North Atlantic Zonal Transect. *Deep Sea Res Part II* 116:303–320. <https://doi.org/10.1016/j.dsr2.2014.11.020>
- Lam PJ, Twining BS, Jeandel C, Roychoudhury A, Resing JA, Santschi PH, Anderson RF (2015b) Methods for analyzing the concentration and speciation of major and trace elements in marine particles. *Prog Oceanogr* 133:32–42. <https://doi.org/10.1016/j.pocean.2015.01.005>
- Lamborg CH, Buesseler KO, Lam PJ (2008) Sinking fluxes of minor and trace elements in the North Pacific Ocean measured during the VERTIGO program. *Deep Sea Res Part II* 55:1564–1577. <https://doi.org/10.1016/j.dsr2.2008.04.012>
- Lee JM, Boyle EA, Echevoyen-Sanz Y, Fitzsimmons JN, Zhang R, Kayser RA (2011) Analysis of trace metals (Cu, Cd, Pb, and Fe)

- in seawater using single batch nitrilotriacetate resin extraction and isotope dilution inductively coupled plasma mass spectrometry. *Anal Chim Acta* 686:93–101. <https://doi.org/10.1016/j.aca.2010.11.052>
- Li Y-H (1981) Ultimate removal mechanisms of elements from the ocean. *Geochim Cosmochim Acta* 45:1659–1664. [https://doi.org/10.1016/0016-7037\(81\)90001-6](https://doi.org/10.1016/0016-7037(81)90001-6)
- Li Q, Cheng H, Zhou T, Lin C, Guo S (2012) The estimated atmospheric lead emissions in China, 1990–2009. *Atmos Environ* 60:1–8. <https://doi.org/10.1016/j.atmosenv.2012.06.025>
- Madison AS, Tebo BM, Mucci A, Sundby B, Luther III GW (2013) Abundant porewater Mn(III) is a major component of the sedimentary redox system. *Science* 341:875–878. <https://doi.org/10.1126/science.1241396>
- Michael SM, Crusius J, Schroth AW, Campbell R, Resing JA (2023) Glacial meltwater and sediment resuspension can be important sources of dissolved and total dissolvable aluminum and manganese to coastal ocean surface waters. *Limnol Oceanogr*. <https://doi.org/10.1002/lno.12339>
- Minami T, Konagaya W, Zheng L, Takano S, Sasaki M, Murata R, Nakaguchi Y, Sohrin Y (2015) An off-line automated preconcentration system with ethylenediaminetriacetate chelating resin for the determination of trace metals in seawater by high-resolution inductively coupled plasma mass spectrometry. *Anal Chim Acta* 854:183–190. <https://doi.org/10.1016/j.aca.2014.11.016>
- Moffett JW, Ho J (1996) Oxidation of cobalt and manganese in seawater via a common microbially catalyzed pathway. *Geochim Cosmochim Acta* 60:3415–3424. [https://doi.org/10.1016/0016-7037\(96\)00176-7](https://doi.org/10.1016/0016-7037(96)00176-7)
- Nakaguchi Y, Sakamoto A, Asatani T, Minami T, Shitashima K, Zheng L, Sohrin Y (2022) Distribution and stoichiometry of Al, Mn, Fe Co, Ni, Cu, Zn, Cd, and Pb in the Seas of Japan and Okhotsk. *Mar Chem*. <https://doi.org/10.1016/j.marchem.2022.104108>
- Nishioka J, Obata H, Ogawa H, Ono K, Yamashita Y, Lee K, Takeda S, Yasuda I (2020) Subpolar marginal seas fuel the North Pacific through the intermediate water at the termination of the global ocean circulation. *Proc Natl Acad Sci USA* 117:12665–12673. <https://doi.org/10.1073/pnas.2000658117>
- Nishioka J, Obata H, Hirawake T, Kondo Y, Yamashita Y, Misumi K, Yasuda I (2021) A review: iron and nutrient supply in the subarctic Pacific and its impact on phytoplankton production. *J Oceanogr* 77:561–587. <https://doi.org/10.1007/s10872-021-00606-5>
- Noble AE, Ohnemus DC, Hawco NJ, Lam PJ, Saito MA (2017) Coastal sources, sinks and strong organic complexation of dissolved cobalt within the US North Atlantic GEOTRACES transect GA03. *Biogeosciences* 14:2715–2739. <https://doi.org/10.5194/bg-14-2715-2017>
- Sim N, Orians KJ (2019) Annual variability of dissolved manganese in Northeast Pacific along Line-P: 2010–2013. *Mar Chem*. <https://doi.org/10.1016/j.marchem.2019.103702>
- Sohrin Y, Bruland KW (2011) Global status of trace elements in the ocean. *TrAC Trends Anal Chem* 30:1291–1307. <https://doi.org/10.1016/j.trac.2011.03.006>
- Spencer D, Bacon M, Brewer P (1981) Models of the distribution of ^{210}Pb in a section across the North Equatorial Atlantic Ocean. *J Mar Res* 39:119–138
- Suzuki K, Liu H, Saino T, Obata H, Takano M, Okamura K, Sohrin Y, Fujishima Y (2002) East-west gradients in the photosynthetic potential of phytoplankton and iron concentration in the subarctic Pacific Ocean during early summer. *Limnol Oceanogr* 47:1581–1594. <https://doi.org/10.4319/lo.2002.47.6.1581>
- Talley LD, Pickard LG, Emery JW, Swift JH (2011) Descriptive physical oceanography: An introduction. Elsevier, Oxford
- Taylor SR (1964) Abundance of chemical elements in the continental crust: a new table. *Geochim Cosmochim Acta* 28:1273–1285. [https://doi.org/10.1016/0016-7037\(64\)90129-2](https://doi.org/10.1016/0016-7037(64)90129-2)
- Thunell R, Tappa E, Varela R, Llano M, Astor Y, Muller-Karger F, Bohrer R (1999) Increased marine sediment suspension and fluxes following an earthquake. *Nature* 398:233–236. <https://doi.org/10.1038/18430>
- Wong KH, Nishioka J, Kim T, Obata H (2022) Long-range lateral transport of dissolved manganese and iron in the subarctic Pacific. *J Geophys Res Oceans*. <https://doi.org/10.1029/2021jc017652>
- Wu J, Boyle E, Sunda W, Wen L-S (2001) Soluble and colloidal iron in the oligotrophic North Atlantic and North Pacific. *Science* 293:847–849. <https://doi.org/10.1126/science.1059251>
- Wuttig K, Townsend AT, van der Merwe P, Gault-Ringold M, Holmes T, Schallenberg C, Latour P, Tonnard M, Rijkenberg MJA, Lannuzel D, Bowie AR (2019) Critical evaluation of a seaFAST system for the analysis of trace metals in marine samples. *Talanta* 197:653–668. <https://doi.org/10.1016/j.talanta.2019.01.047>
- Yasuda T, Kitamura Y (2003) Long-term variability of North Pacific subtropical mode water in response to spin-up of the subtropical gyre. *J Oceanogr* 59:279–290. <https://doi.org/10.1023/A:1025507725222>
- Zheng L, Sohrin Y (2019) Major lithogenic contributions to the distribution and budget of iron in the North Pacific Ocean. *Sci Rep* 9:11652. <https://doi.org/10.1038/s41598-019-48035-1>
- Zheng L, Minami T, Takano S, Minami H, Sohrin Y (2017) Distribution and stoichiometry of Al, Mn, Fe Co, Ni, Cu, Zn, Cd, and Pb in seawater around the Juan de Fuca Ridge. *J Oceanogr* 73:669–685. <https://doi.org/10.1007/s10872-017-0424-2>
- Zheng L, Minami T, Konagaya W, Chan C-Y, Tsujisaka M, Takano S, Norisuye K, Sohrin Y (2019) Distinct basin-scale-distributions of aluminum, manganese, cobalt, and lead in the North Pacific Ocean. *Geochim Cosmochim Acta* 254:102–121. <https://doi.org/10.1016/j.gca.2019.03.038>
- Zheng L, Minami T, Takano S, Sohrin Y (2022) Distributions of aluminum, manganese, cobalt, and lead in the western South Pacific: interplay between the South and North Pacific. *Geochim Cosmochim Acta* 338:105–120. <https://doi.org/10.1016/j.gca.2022.10.022>
- Zurbrick CM, Gallon C, Flegal AR (2017) Historic and industrial lead within the Northwest Pacific ocean evidenced by lead isotopes in seawater. *Environ Sci Technol* 51:1203–1212. <https://doi.org/10.1021/acs.est.6b04666>